

On the Origin of Radial Magnetic Fields in Young Supernova Remnants

Byung-Il Jun ¹ and Michael L. Norman

Laboratory for Computational Astrophysics

National Center for Supercomputing Applications

Department of Astronomy, University of Illinois at Urbana-Champaign
5600 Beckman Institute, 405 North Mathews Avenue, Urbana, IL 61801

Received 20 March 1996; accepted 13 June 1996

Accepted for publication in the *Astrophysical Journal*

¹present address: Department of Astronomy, University of Minnesota, 116 Church Street,
S.E., Minneapolis, MN 55455, bjun@astro.spa.umn.edu

ABSTRACT

We study the radio emission from young supernova remnants by means of 3D numerical MHD simulations of the Rayleigh-Taylor instability in the shell of the remnant. The computation is carried out in spherical polar coordinates (r, θ, ϕ) by using a moving grid technique which allows us to finely resolve the shell. Three-dimensional result shows more turbulent (complex) structures in the mixing region than the two-dimensional result, and the instability is found to deform the reverse shock front. Stokes parameters (I, Q, and U) are computed to study the radio properties of the remnant. The total intensity map shows two distinctive regions (inner and outer shells). The inner shell appears to be complex and turbulent exhibiting loop structures and plumes as a result of the Rayleigh-Taylor instability, while the outer shell is faint and laminar due to the shocked uniform ambient magnetic fields. The inner shell resembles the observed radio structure in the main shell of young SNRs, which is evidence that the Rayleigh-Taylor instability is an ongoing process in young SNRs. When only the peculiar components of the magnetic fields generated by the instability are considered, the polarization B-vector in the inner radio shell is preferentially radial with about $20 \sim 50\%$ of fractional polarization which is higher than the observed value. The fractional polarization is lowest in the turbulent inner shell and increases outward, which is attributed to the geometric effect. The polarized intensity is found to be correlated with the total intensity. We demonstrate that the polarized intensity from the turbulent region can dominate over the polarized intensity from the shocked uniform fields if the amplified field is sufficiently strong. Therefore, we conclude that the Rayleigh-Taylor instability can explain the dominant radial magnetic field in the main shell of young supernova remnants. However, the outer faint shell shows

a dominant tangential field orientation due to the shock-compression because this region is not mixed by the Rayleigh-Taylor instability, which is contrary to observations. Therefore, another mechanism is necessary to produce the radial components of the magnetic field at the outer shock, which we suggest a clumpy medium model.

Subject headings: magnetic fields – methods: numerical – MHD – shock waves – supernova remnants

1. Introduction

Radio polarization studies (Milne 1987, Dickel *et al.* 1991) of the synchrotron emission from supernova remnants (SNR) have revealed a curious regularity: young SNRs possess a predominantly radial magnetic field structure, whereas older remnants display circumferential fields consistent with simple compression of the interstellar magnetic field by the supernova shock wave. The origin of radial B-fields in young SNRs, however, has remained a mystery. One suggestion by Gull (1973,1975) is that the interstellar field is ”combed out” radially by dense fingers of stellar ejecta produced by the Rayleigh-Taylor (R-T) instability acting on the decelerating contact surface between the stellar ejecta and swept-up ambient gas. This is the third in a series of papers in which we explore this suggestion via multidimensional numerical MHD simulations.

In a first paper (Jun *et al.* 1995; Paper I) we simulated the classical R-T instability in incompressible magnetized fluids and showed that strong magnetic field components aligned with the gravity vector are produced in the unstable mixing layer separating dense and light fluids. Initially weak magnetic fields are amplified and aligned as they are stretched around dense, downward-plunging R-T fingers. In a second paper (Jun & Norman 1996; Paper II, but see also Jun & Norman 1995) we simulated the evolution of a supernova remnant in two spatial dimensions in a uniform magnetized medium. Because the shell is strongly decelerated as it sweeps up mass, the effective gravity vector is radially outward, and consequently the dense R-T fingers point outward (cf. Fig. 2a). Just as in the classical instability, our simulation showed that the swept-up magnetic field is strongly amplified as field lines drape around these fingers, and that the strongest magnetic field components are indeed radial. However, we could not address in 2D whether these strong radial field components, when seen in projection through a three-dimensional remnant, would produce a net radial B-vector polarization, nor could we address the fractional polarisation of the

radio emission. Nonetheless, our simulation successfully reproduced the observed clumpy radio and X-ray shell which is due to the turbulent structure of the mixing layer.

In this paper, we remove the limitations imposed by 2D axisymmetric calculations and present results of a fully three-dimensional numerical MHD simulation of a supernova remnant. The simulation, described in Section 2, employs a moving Eulerian grid technique which allows us to maintain high numerical resolution in the region of interest—the shell. The 3D simulation is carried out at the same numerical resolution as the 2D simulation reported in Paper II, allowing us to directly compare the nonlinear structures produced by the R-T instability in 2D and 3D (Section 3). In Section 4 we present our detailed study of the radio emission. The Stokes I, Q and U parameters for the synchrotron emission are integrated through the remnant using the self-consistently computed magnetic field distribution and simple assumptions about the spatial distribution of relativistic electrons. From these we compute the total and polarized radio intensity and the polarization fraction of the simulated remnant which we compare with observed remnants. Section 5 provides a further discussion on the polarized radio emission and the origin of the observed dominant radial magnetic field in young SNRs. Our results show that the R-T instability can produce the radial magnetic polarization in the inner region of the remnant if the amplified magnetic field is sufficiently strong. We then discuss the limitations of our model and suggest the necessity for an additional mechanism to produce the radial magnetic fields seen in the outer region of the shell just inside the outer shock wave. Finally, our conclusions are presented in Section 6.

2. Numerical Simulations

We compute the evolution of the SNR in spherical polar geometry using the moving grid technique discussed in Paper II to maintain high resolution in the intershock region.

The numerical method that we use here is the same as in our previous 2D calculation. We take as the computational domain, $67.5^\circ \leq \theta \leq 112.5^\circ$ and $67.5^\circ \leq \phi \leq 112.5^\circ$, and $0 \leq r \leq 1.05r_{shock}$ as illustrated in Figure 1. The intershock region is resolved with $100 \times 200 \times 200$ cells uniformly. The region inside the reverse shock is resolved with eighty ratioed radial zones (i.e.; $80 \times 200 \times 200$ cells) which increase in size as $r \rightarrow 0$ in order to avoid a too stringent Courant condition on the timestep. Periodic boundary conditions across each angular boundary are assumed and reflecting boundary condition at $r = 0$ is used. The outer boundary condition is updated every timestep with the background condition.

The initial conditions for the physical variables in this calculation are also identical to those used in Paper II permitting a direct comparison of 2D and 3D results. A supernova explosion is initialized by depositing a kinetic energy of 10^{51}ergs inside a radius of 0.1pc with an assumption that the velocity is linearly proportional to the radius. The outer $3/7$ of the ejecta mass $1.4 M_\odot$ is distributed with a power law density profile $\rho \sim r^{-7}$ and the mass distribution of the inner $4/7$ of the ejecta is assumed to be constant in order to mimic Type-Ia supernova remnants (Colgate & McKee 1969). We assume a uniform background density of $1.67 \times 10^{-24} \text{g/cm}^3$ (The evolution of SNR in a nonuniform background density has been modeled recently by Jun (1995) and will be presented in a subsequent paper.). The initial temperature of the gas is assumed to be 10^4K everywhere. The initial magnetic field is chosen to be tangential to the $\theta - \text{direction}$ lying in the $r - \theta$ plane with strength $3.5 \mu\text{G}$. We perturb the entire space with a random noise of 2.0% amplitude of the density field to trigger the R-T instability in the region near the contact discontinuity.

The above initial state is evolved by solving the ideal compressible MHD equations on a moving Eulerian grid using the ZEUS-3D code developed at the Laboratory for Computational Astrophysics at the University of Illinois, Urbana-Champaign (Clarke & Norman 1994). The code uses von Neumann-Richtmyer artificial viscosity to stabilize

shocks. Fluid is advected through the mesh using the upwind, monotonic interpolation scheme of van Leer (second order) advection. Magnetic fields are transported by Constrained Transport (Evans & Hawley 1988) modified with the Method of Characteristics (Stone & Norman 1992, Hawley & Stone 1995). Because we simulate strong shocks, the Courant time for artificial viscosity is the smallest time step. Therefore we sub-cycle the viscous routine which saves CPU by about a factor of two by avoiding redundant calculation. The code runs efficiently with an average zone-cycles per second rate of 1.27×10^5 and about 420 MFLOPS (mega floating point operations per second) on one processor of a Cray C90 machine. The code is further optimized to run in parallel using 16 processors of the Cray C90 machine by microtasking.

3. Growth of R-T instability in Three Dimensions

Rather than repeating the basic features of the nonlinear R-T instability in two dimensions, we focus on new results by comparing the 3D results to the 2D simulation done with the same mesh resolution. Readers are referred to Paper II for the detailed study of the R-T instability in two dimensions. Figure 2 shows grey scale images of density at $t=100,200,300,400$, and 500 years from top to bottom. Proceeding from the outside inward on any panel, we see the basic structure of a SNR shell in the decelerating phase : undisturbed ambient gas (light grey); forward shock; shocked ambient gas (medium grey); mixing layer/stellar ejecta (black); reverse shock and unshocked stellar ejecta (light grey). The most obvious difference is that the 3D result shows more small-scale structure in the dense fingers of stellar ejecta. This result was also found in our 2D and 3D simulations of the classical R-T instability discussed in Paper I. In general, the largest wavelength present at any given time is similar in both 2D and 3D. However, just as we found before, the largest wavelength increases and the R-T fingers become longer as the remnant evolves

beyond the self-similar stage. Another noticeable result is that some bubbles of shocked ambient gas grow up to the reverse shock front and deform it. In the 3D simulation, the deformation of the reverse shock is more severe at 100 and 200 years. The stronger deformation of the reverse shock at this early stage is due to the stronger deceleration of the ejecta. However, the deformation of the reverse shock by the R-T bubbles is less pronounced in a 2D simulation of higher resolution 300x400 (Paper II). As we learned from our study of the classical R-T instability, the kinetic energy increases as the resolution decreases. At low resolution, small scales which are responsible for the dissipation of turbulent kinetic energy are not resolved. Therefore, we believe the deformation of the reverse shock is likely due to a resolution effect. However, whether this deformation will disappear in high resolution 3D simulations is not yet clear. The observational consequence of this feature is possibly a broader radio shell.

Figure 3 compares the angle-averaged radial profile of magnetic field strength through the remnant in 1D, 2D, and 3D simulations. The thickness of the mixing layer is comparable in 2D and 3D contrary to our results of the classical R-T instability in which the 3D simulation produced a 40 % thicker mixing layer than in 2D. In the latter case, this effect is due to longer fingers being produced in 3D than in 2D. As explained in Paper I, the interaction and merging between the fingers is reduced in 3D due to the extra degree of freedom than in 2D. The tendency of merging in 2D occurs due to an inverse cascade of turbulent energy (Kraichnan & Montgomery 1979). Therefore, fingers in 3D can grow more easily without much loss of kinetic energy. Why then is this effect not seen in the SNR simulations? The comparable thickness of the mixing layer between 2D and 3D in the SNR simulation may be explained by three effects. First, the wavelength of R-T fingers under the conditions present in SNRs has grown to its maximum size. The dominant wavelength ceases to grow any further after about 200 years (see Fig.2). The maximum size of the wavelength is likely restricted by the finite thickness of the intershock region

and the finite region between the reverse shock and the contact discontinuity. Chevalier (1982) found that the thickness between the contact discontinuity and the reverse shock decreases as n (the power law index of the expanding ejected material) increases. Later, the dominant wavelength was found to decrease as n increases (Chevalier *et al.* 1992). Second, the thickness of the heavy fluid region was assumed to be infinite in our simulations of the classical R-T instability, whereas it is finite in the SNR case. Therefore, in the former case the dominant wavelength can become larger and larger without limit with a continuous interaction between fingers as it evolves. In the SNR case, the interaction between fingers is very weak after the R-T fingers reach the maximum wavelength. As a result, the effect of the higher degree of freedom in 3D is not significant from the standpoint of the mixing layer. Third, it is likely that the growth of the R-T finger is hindered by the high density region behind the forward shock in the case of SNR (cf. Fig. 2 in Paper II).

Both 2D and 3D simulations produce a strong magnetic field layer near the contact discontinuity. The *average* magnetic field strength ($\sim 1.5 \times 10^{-5} \text{gauss}$) is higher than the shocked ambient field but much lower than the equipartition field estimate of $10^{-4} \sim 10^{-3} G$ (*e.g.*, see Strom & Duin 1973, Henbest 1980, Anderson *et al.* 1991) inferred in young radio SNR. Numerically, the magnetic field strength in the mixing layer is found to increase with higher grid resolution because the effect of higher resolution is to decrease the numerical dissipation and enhance the turbulent amplification of the field (*e.g.* see Figs 19 and 20 in Paper I). A resolution study in 3D is highly desirable as a future project. In order to confront observations of radio SNRs on a quantitative level, the accurate estimation of the field strength is required.

To study the evolution of both fluid and magnetic fields in the mixing layer, the time history of the turbulent kinetic and magnetic energy densities is shown in Figure 4 for both 2D and 3D simulations. The resolution of the 2D simulation (180x200) is the same as

the 3D (180x200x200). Turbulent energy density is defined as the peculiar kinetic energy density computed by excluding the contribution from pure radial expansion of the SNR (i.e.; $E_{tur} = \frac{\int \frac{1}{2}\rho|\vec{v}-\langle\vec{v}\rangle_{\theta,\phi}|^2dV}{\int dV}$) and the magnetic energy density is also computed by taking the peculiar component to include only the magnetic field amplified by the instabilities ($E_{mag} = \frac{\int \frac{1}{8\pi}|\vec{B}-\langle\vec{B}\rangle_{\theta,\phi}|^2dV}{\int dV}$) where $\langle\vec{v}\rangle_{\theta,\phi}$ and $\langle\vec{B}\rangle_{\theta,\phi}$ are the angle-averaged values of \vec{v} and \vec{B} (the angle-averaged value is found to be close to the 1D result). First of all, the radial components of turbulent and magnetic energy densities are dominant in both 2D and 3D. All components grow rapidly at first due to rapid growth of the R-T instability during the initial strong deceleration phase (cf. Fig.5, Paper II). After the first rapid rise, the turbulent energy density (particularly the radial component) decreases dramatically due to the weak deceleration and the shell expansion. Therefore, the maximum turbulent energy density is set by the highest growthrate of the R-T instability in the early stage when the deceleration is strongest. We find one new result here by comparing the 2D and 3D results. The radial component of turbulent energy density in 3D is found to be greater than in 2D until about 200 years, and thereafter it becomes smaller. This crossover effect also appears in the evolution of the magnetic energy density although crossover occurs somewhat later: at about 320 years. In comparison, in our simulation of the classical R-T instability (Paper I) the energy density in 3D was found to always be greater than in 2D except for one simulation. This difference can be explained as follows. In the early stage of evolution, the interaction and merging between R-T fingers is very strong until the wavelength reaches the maximum size which is controlled by the thickness of intershock region and the thickness between the contact discontinuity and the reverse shock. The interaction between R-T fingers is greater in 2D due to the lower degree of freedom (symmetry restriction) than in 3D. Thus, the reduced interaction between fingers in 3D results in more active growth of the instability than in 2D. Once the maximum size of the wavelength is reached, this effect is no longer important. Now more efficient dissipation due to the small scale structures

in 3D than in 2D results in the smaller energy in 3D at late times. About 0.57% of total initial kinetic energy transferred into the total turbulent energy by the end of simulation (t=500 years). The instability converted about 0.0011% of the initial kinetic energy into the magnetic energy while the total magnetic energy including shock-compressed field reached about 0.002% of the initial kinetic energy. The energy conversion into the magnetic energy by the instability seems very low. However, we expect from the previous studies (Paper I & II) that a higher resolution simulation will increase the magnetic energy and decrease the turbulent energy.

4. Radio Emission

In order to compute the radio emission from the remnant, we make a few necessary assumptions. We assume synchrotron radiation is solely responsible for the radio emission from young SNRs. We take as the radio emissivity the expression (Clarke *et al.* 1989)

$$i(\nu) = C_1 \rho^{1-2\alpha} p^{2\alpha} (B \sin \psi)^{\alpha+1} \nu^{-\alpha} \quad (1)$$

where ρ is the gas density, p is the gas pressure, B is the magnetic field strength, ψ is the angle between the local B field and the line of sight, ν is the frequency of radiation, α is the spectral index, and C_1 is a proportionality constant which depends on the normalization of the relativistic electron energy distribution function and assumed to be 1. Since we are not evolving the relativistic electron population self-consistently, we assume that the spectral index is uniform everywhere and taken as 0.6. In the derivation of this expression, we have made an assumption that the number density of the relativistic electrons has a power law spectrum. In addition, the fraction of relativistic electrons in the fluid is an unknown constant which will determine the amplitude of the emissivity. A better modeling of radio emission will require the accurate evolution of the relativistic electrons including proper acceleration processes such as the diffusive shock acceleration, which is beyond the scope of

this paper.

4.1. Total Intensity

To compute the total radio intensity (Stokes parameter I), we integrate the emissivity along the line of sight. Since our numerical simulation is carried out in a 45 degree wedge in the range, $\theta = 67.5^\circ \sim 112.5^\circ$ and $\phi = 67.5^\circ \sim 112.5^\circ$, the 3D data is replicated every 45 degrees from $\phi = 0^\circ \sim 180^\circ$ along the ϕ -direction and then integrated along the X-direction to obtain the total intensity (see Fig. 1; hereafter we call this the normal case.). Figure 5 illustrates the total radio intensity at $t=200,300,400,$ and 500 years. Note that only a 45 degree sector of the image shows the total intensity map which is truly integrated through the entire remnant. The radio shell imaged in the total intensity shows two distinctive regions : the inner turbulent shell and the outer faint laminar shell. Already at 200 years, the bright clumpy inner shell is clearly seen, which is the consequence of the amplified magnetic fields by the R-T instability. The clumpy inner shell contains many turbulent structures such as loops and plumes. These loops result from the strong magnetic fields lines draped around the R-T fingers as they grow. On the other hand, the outer faint shell results from the shock-compressed uniform ambient fields. The maps at $t= 400$ and 500 years show a thicker radio shell than at earlier times. The loop structures are larger at later times. The inner turbulent shell in our simulated total intensity map is remarkably similar in appearance to the main shell in young SNRs such as Tycho or the ring in Cas A, which is compelling evidence for the R-T instability in young SNRs.

The radio emissivity depends on the angle (ψ) between the local B vector and the viewing angle. The smooth radio emission behind the main shock is large because in this projection $\psi = 90$. To examine the effect of ambient magnetic field orientation on the total radio intensity, we show the total intensity integrated along the Z-direction (i.e., $\psi = 0$).

Replication of our 3D data in the θ -direction up to the pole is not a good way to produce the total intensity map because we have no information near the pole. Instead, we switch the magnetic field components (B_ϕ and B_θ) to mimic the situation where the magnetic field is originally initialized along the ϕ -direction (hereafter we call this switch-B case). The total intensity map produced in this way is illustrated in Figure 6b (for the amplitude, see Fig. 11). The total intensity near the outer shock is very faint while the main shell remains bright. To assess the contribution of the instability-amplified fields to the emission, Figure 6c shows the total intensity map generated by the peculiar components of magnetic fields (hereafter we call this peculiar-B case). The peculiar components are defined as $B_{pec} = B - B_{avg}$ where B_{avg} is the averaged magnetic field over the angular direction. Thus, the peculiar components are purely the result of the instability. The peculiar-B case looks generally similar to the switch-B case but the outer shock is not seen in the peculiar-B case. The total intensity is fainter overall than the switch-B case because we have removed the contribution from the shocked mean magnetic fields.

4.2. Polarized Intensity

To compute the polarized emission, we compute the Stokes Q and U parameters as follows (Clarke *et al.* 1989)

$$Q(\nu) = \int i(\nu) f_o \cos 2\chi dl \quad (2)$$

$$U(\nu) = \int i(\nu) f_o \sin 2\chi dl \quad (3)$$

where χ is the position angle of the local B field projected in the plane of the sky, dl is the increment along line of sight and f_o is the degree of linear polarization of the accumulated radiation for an ensemble of electrons with an energy power law index x that spiral about a

uniform magnetic field with an isotropic distribution of pitch angles. f_o is given by

$$f_o = \frac{x+1}{x+7/3} = \frac{\alpha+1}{\alpha+5/3} \quad (4)$$

The linearly polarized intensity and the net polarization angle are obtained by

$$P = \sqrt{Q^2 + U^2} \quad (5)$$

$$\chi_0 = \frac{1}{2} \tan^{-1} \frac{Q}{U} \quad (6)$$

respectively.

Figure 7 shows the polarized intensity (top panel) and the polarization B-vector (bottom panel) at $t = 500$ years (for the amplitude, see Fig. 11). The vector length is proportional to the polarized intensity; the sign of the vector direction is arbitrary. The polarized intensity is found to be very high in the outer shell where the polarization B-vector is dominantly tangential. The dominant tangential magnetic field is simply due to the initial direction of the ambient magnetic field. Because the mixing layer does not extend all the way to the outer shock, the shock-compressed ambient field remains uniform. When a line-of-sight integration is performed, those uniform magnetic fields dominate the polarization over the turbulent magnetic fields in the mixing layer. Consequently, the polarization B-vector is sensitive to the viewing angle. Magnetic fields in the main turbulent shell shows some deviation from the tangential direction, but they are not strong enough to dominate over the shocked uniform fields (we discuss this issue further in section 5.). Figure 8 shows the polarization for the switch-B case. In general, the polarization B-vector is radial and the polarized intensity is strong in the inner main shell. Again, the laminar post-shock magnetic field is dominating the turbulent fields. We then ask : what would the remnant look like if the ambient field were completely disordered at the outer shock by some mechanism in order to exclude the shock-compression of uniform ambient field ? To approximate this without running a new simulation, consider Figure 9, which shows the

polarization for the peculiar-B case. We see the main shell is highly polarized; the degree of linear polarization is about $20 \sim 50\%$. This range is somewhat high in comparison with the degree of linear polarization observed in the main shell of Tycho’s SNR, 7%. However, a disordered ambient field whose contribution we have ignored here would increase the unpolarized emission, thus decreasing the fractional polarization. Also, the polarization is likely to decrease in a more turbulent flow which can be achieved by a higher numerical resolution simulation. The polarization B-vectors illustrate dominant radial magnetic fields.

In general, the total intensity appears to be well correlated with the polarized intensity in the main turbulent shell (e.g. compare Fig.6(c) and Fig.9). Figure 10 shows the distribution of the polarized intensity with the total intensity in the peculiar-B case. The upper limit of the slope is about 0.5 (the theoretical upper limit is 0.7 for a uniform magnetic field and $\alpha = 0.6$). The correlation between the polarized intensity and the total intensity implies that the flow contains a characteristic scale carrying strong magnetic fields or the flow is not highly turbulent. In our simulation (peculiar-B case), the stretched magnetic fields by the R-T fingers are more responsible for a strong radio emission. Therefore it is likely that the total intensity is well correlated with the polarized intensity on the R-T finger scale as long as the R-T fingers maintain their coherent structures containing strong magnetic fields. However, numerical resolution is an important factor for the development of turbulence because the higher resolution increases the numerical Reynolds number. At a higher resolution, we anticipate the fractional polarization will decrease due to a higher cancellation of magnetic field directions as the flow becomes highly turbulent. It is unclear yet whether the R-T fingers will remain coherent and carry dominant magnetic fields at higher resolution. It would be worthwhile to study the correlation between the polarized intensity and the total intensity as a function of wavelength for both the simulated data at various grid resolutions and the observed data.

The radial distribution of total and polarized intensity and fractional polarization are shown in Figure 11. In each case, we show the central slice from the images in Figure 9. The normal case and peculiar-B case show the thick shell near the outer shock while it is hard to identify the shell in switch-B case. This is because the brightness originating from the shocked uniform field in the switch-B case decreases with the radius. The shell can be identified better in the overall image of total intensity (see Fig.6b). The normal case and switch-B case show the jump in fractional polarization between the inner turbulent shell and the outer laminar shell. Note that the brightness in the peculiar-B case is lower than the normal case because we removed the uniform magnetic field components. Fractional polarization is generally high in the entire region and it shows the lowest degree in the inner turbulent shell region. From the turbulent region, the fractional polarization increases outward. This tendency is observed in Cas A (Anderson *et al.* 1995) and Tycho (Dickel *et al.* 1991). This could be explained by the geometric effect. The integration along the line of sight near the turbulent shell will sum up the magnetic field vector destructively while this destruction will decrease with the larger radius due to the smaller overlap of the turbulent region along the line of sight.

4.3. Radio Luminosity

The time history of the radio luminosity is shown in Figure 12. The radio luminosity is computed by integrating the radio emissivity over the computational space. The integration is carried out along lines of sight parallel to the X,Y,and Z-directions (see Fig. 1), which we denote L_x , L_y , and L_z , respectively. Also plotted in Fig.12 are $L_{x,\delta B}$, $L_{y,\delta B}$,and $L_{z,\delta B}$ which stand for the radio luminosity integrated along X, Y, and Z-directions, with the peculiar components of magnetic fields. Generally, all curves show the same features in which the time derivative of luminosity changes from positive to negative at about 300 years. The

different amplitude of the curves is due to the different lines of sight relative to the ambient field, which strongly influence the total luminosity. The effect of a different line-of-sight to the luminosity will become less important as the flow becomes more turbulent and the field amplification increases. Our 3D result agrees with our previous 2D simulation (Paper II) except for the earlier change of the slope.

5. Radial Magnetic Field in the Shell

Overall, our peculiar-B case more closely resembles observed radio SNRs than do the cases which include the emission from a uniform magnetic field. Thus, the results of our polarization study issue some constraints on the origin of the observed dominant radial field in young SNR. If viewing angle and shocked uniform ambient fields are the main factors for the polarization as we found, the polarization B-vector of all young SNRs should not necessarily be radial. Various distributions of B-vector including tangential fields should be observed. However, as Milne(1987) found in his polarization surveys of SNRs, the projected fields in all measured young SNRs are predominantly radial. These apparently conflicting results may be resolved by one or more of the following effects absent from our simulation: (1) field amplification in the mixing layer may be larger than we calculate; (2) the uniformity of the post-shock field may be lower than we calculate because the ambient field is non-uniform ; or (3) an additional mechanism (instability) operates at the shock front which reduces the uniformity of the post-shock field. We discuss these possibilities in turn.

Let's first consider the magnetic field distribution in the inner shell where the flow is mixed by the R-T instability. Our simulation shows that the polarization angle in the inner shell is dependent on the viewing angle. This is because the emission from the amplified magnetic fields in the mixing layer is not dominant over the emission from the shocked

uniform magnetic fields in the outer shell. The degree of amplification of the magnetic fields in the shell is limited by our numerical resolution. The maximum field strength obtained is only about 90 times higher than the ambient magnetic field. However, this amplification occurs very locally and the angle-averaged magnetic field strength peaks at about $1.5 \times 10^{-5} \textit{gauss}$, only 5 times higher than the ambient field (see Fig. 3). The observed magnetic field in young SNR is much stronger than our simulated value. A minimum energy estimate gives a magnetic field strength, $B = 10^{-4} \sim 10^{-3} \textit{gauss}$ throughout the shell of the remnant although the minimum energy requirement (close to equipartition assumption) is not well justified. Without an assumption of the equipartition, Cowsik & Sarkar (1980) estimated the lower limit to the magnetic field in Cas A, $8 \times 10^{-5} \textit{gauss}$, assuming that the bremsstrahlung by the electrons responsible for the non-thermal radio emission does not exceed the upper limit on the γ -ray flux. Also, Matsui et al. (1984) used the mean electron density inferred from an analysis of X-ray fluxes to estimate the magnetic field in Kepler’s SNR, $7 \times 10^{-5} \textit{gauss}$ from the observed rotation measure. These values are weaker than the equipartition magnetic field but certainly stronger than the shocked ambient field and our simulated value. Now, we ask whether the polarized intensity in the inner turbulent shell could become dominant over the polarized intensity from the shocked uniform magnetic fields behind the outer shock front as the amplified field strength increases. Since the polarized intensity is a fraction of total intensity, one can roughly write ignoring the distribution of relativistic electrons

$$\frac{P_c}{P_a} \equiv \frac{f_c I_c}{f_a I_a} \simeq \frac{f_c B_c^{1+\alpha}}{f_a B_a^{1+\alpha}} \quad (7)$$

where P , I , and f represent the polarized intensity, the total intensity, and the fractional polarization, and subscripts c and a denote quantities originating from the shock-compressed uniform magnetic fields and the amplified magnetic fields by the R-T instability, respectively. The fractional polarization for the uniform magnetic field is 0.7 from equation(4). The fractional polarization from the amplified magnetic field in our simulation is about 0.2 to

0.5. However, it is much lower in the real SNRs. We choose $f_a = 0.05$ which is an observed fractional polarization in the ring of Cas A (e.g. see Anderson et al.(1995). Then one obtains the critical value of amplified magnetic field, $B_a \approx 5 \times B_c$, after taking $\frac{P_c}{P_a} \approx 1$ and $\alpha = 0.6$. This critical strength of amplified magnetic field is weaker than the estimated lower limit to the magnetic field in Cas A. Therefore, the shocked uniform magnetic field will not be able to dominate over the amplified magnetic field in the inner shell if the amplified magnetic field is higher than the critical value. It should be noted that this critical value is only a rough estimate because the number density of relativistic electrons is assumed to be constant throughout the remnant and the fractional polarization from the amplified magnetic field is uncertain. A possible high acceleration efficiency of electrons at the shock will increase our estimated critical value of the magnetic field.

In order to check the validity of the above discussion, we study the radio emission with our simulated data under the assumption of higher amplification of the field. We compute the emissivity by giving a multiplication factor 5 to magnetic field components stronger than the shock-compressed field. This is to mimic the situation that the field amplification by the instability is five times higher than our simulation. Figure 13 shows the total intensity (top panel) and the polarized intensity (bottom panel) computed in this way. The inner radio shell in the total intensity is much brighter compared to the faint outer shell. Bottom panel shows the polarized intensity overlaid with the polarization B-vector. The polarized intensity in the inner shell now dominates over the outer shell so that the field distribution in the inner shell is no longer tangential. Magnetic fields in the inner shell shows turbulent structure with preferentially radial components while the outer shell still shows tangential fields. Therefore, we conclude that the R-T instability can explain the dominant radial magnetic fields in the inner shell provided the field amplification is high enough.

Although the radial B-vector polarization in the inner shell can be produced by the R-T instability, B-vector polarization in the undisturbed region (outer shell) between the outer shock and the tip of the R-T fingers remains dependent on the viewing angle if the ambient magnetic fields are uniform. Even if the ambient magnetic fields are not uniform but tangled, B-vector polarization in the faint outer shell should be preferentially tangential due to the shock-compression. The undisturbed region is about as wide as the region mixed by the R-T instability so that it will produce an extended radio shell outside the inner radio shell with tangentially polarized B-vector (e.g. see Figs. 6a, 7, and 13). However, radial magnetic fields are observed in the entire radio shell up to the outer shock in young SNRs (*e.g.*, Dickel *et al.* 1991 for Tycho’s SNR). Therefore, our results show that it is necessary to have an extra mechanism which operates at the outer shock front to produce the dominant radial components of fields. Or at least, the field should be randomized at the outer shock. Then, the radial field may become dominant inward from the shock since the radial components of the field evolve as $B_r \propto \frac{1}{r^2}$ while the tangential components evolve as $B_t \propto \frac{1}{r}$ (cf. Duin & Strom 1975, Reynolds & Chevalier 1981). As suggested in Paper II, a clumpy medium model or shock instability are possible mechanisms to randomise the field. Recently, a clumpy medium model has been simulated to produce encouraging results on this issue (Jun 1995, Jun *et al.* 1996).

6. Conclusions

We have carried out a self-consistent MHD simulation of a supernova remnant in the decelerating phase ($0 \leq t \leq 500\text{yrs}$) in three spatial dimensions. Our moving Eulerian grid technique allows us to maintain a high spatial resolution in the shell and accurately model the nonlinear growth and saturation of the Rayleigh-Taylor instability at the interface between the stellar ejecta and swept-up ISM. Ambient magnetic fields are amplified in the

mixing layer produced by the instability by stretching and shearing. The resulting magnetic field distribution is used to compute synthetic radio maps of total and polarized intensity as well as fractional polarization which can be compared with observation.

Our 3D MHD simulation produces a clumpy thick radio shell which includes loop structures and plumes. In our simulation, the radio shell can be characterized by two distinctive regions according to the total intensity : a bright, clumpy, inner shell corresponding to the turbulent mixing layer and an outer faint shell originating from the shocked uniform fields. The inner shell in the simulated total intensity map is remarkably similar to the main radio shell in young SNRs such as Tycho and the ring in Cas A, which suggests that the R-T instability in the shell of young SNRs is indeed an ongoing process. The map of polarization angle exhibits a dominant radial magnetic field in a main turbulent shell when only the peculiar component of the magnetic fields are included in the emissivity. The degree of linear polarization in the inner shell is found to be about $20 \sim 50\%$ which is higher than the observed value in young SNR. The fractional polarization is the lowest in the turbulent region because of the highest cancellation of magnetic fields. And it increases outward, which is attributed to the geometric effect. The polarized intensity is well correlated with the total intensity. It is possible that a good correlation between the polarized intensity and the total intensity occurs because the flow is not highly turbulent due to our limited resolution. When we consider all magnetic field components in the intershock region, the polarization B-vector in the inner turbulent shell is found to be viewing angle dependent because of an undistorted uniform tangential magnetic field near the outer shock front. However, this is very likely due to the insufficient amplification of the field in our simulation possibly by the limited numerical resolution. We demonstrated that the amplified magnetic field in the turbulent region could dominate in the polarized intensity over the shocked uniform field if the amplified magnetic field is sufficiently strong. We conclude that the R-T instability can explain the dominant radial magnetic fields in the

inner shell of young SNRs. On the other hand, the radio polarization of outer faint shell is found to be viewing angle dependent if the ambient magnetic field is uniform, because that region is not disturbed by the R-T instability. Even if the ambient magnetic field is not uniform but disordered on scales smaller than the SNR's shell, this faint outer shell will always show the dominant tangential components of polarization B-vectors, contrary to what is observed. Therefore, our results suggest that an extra mechanism is required to generate radial magnetic fields at the outer shock front.

We thank Roger Chevalier, John Dickel, and Tom Jones for helpful discussions. We are grateful for very useful discussions on the polarization of radio emission with Larry Rudnick. We also thank the referee, John Blondin for useful comments. The simulations were performed on the Cray C90 at Pittsburgh Supercomputing Center. B.-I. J. was partly supported at the University of Minnesota by NSF grant AST-9318959 and by the Minnesota Supercomputer Institute.

REFERENCES

- Anderson, M., Rudnick, L., Leppik, P., Perley, R., & Braun, R. 1991, *ApJ*, 373, 146
- Anderson, M., Keohane, J.W., & Rudnick, L. 1995, *ApJ*, 441, 300
- Chevalier, R.A. 1982, *ApJ*, 258, 790
- Chevalier, R.A., Blondin, J.M., & Emmering, R.T. 1992, *ApJ*, 392, 118
- Clarke, D.A., Norman, M.L., & Burns, J.O. 1989, *ApJ*, 342, 700
- Clarke, D.A. & Norman, M.L. 1994, NCSA Technical Report #15,
<http://zeus.ncsa.uiuc.edu:8080/lca/zeus3d/zeus32.ps>
- Colgate, S.A. & McKee, C. 1969, *ApJ*, 157, 623
- Cowsik, R. & Sarkar, S. 1980, *MNRAS*, 191, 855
- Dickel, J.R., van Breugel, W.J.M., & Strom, R.G. 1991, *AJ*, 101, 2151
- Duin, R.M. & Strom, R.G. 1975, *A&A*, 39,33
- Evans, C.R. & Hawley, J. F. 1988, *ApJ*, 332, 659
- Gull, S.F. 1973, *MNRAS*, 161, 47
- Gull, S.F. 1975, *MNRAS*, 171, 263
- Hawley, J.F. & Stone, J.M. 1995, *Comput. Phys. Comm.*, 89, 127
- Henbest, S. N. 1980, *MNRAS*, 190, 833
- Jun, B.-I. 1995, Ph.D. thesis, Univ. Illinois
- Jun, B.-I., Jones, T.W., & Norman, M.L. 1996, *ApJ*, accepted

Jun, B.-I. & Norman, M.L. 1995, *Ap&SS*, 233, 267

Jun, B.-I. & Norman, M.L. 1996, *ApJ*, accepted

Jun, B.-I., Norman, M.L., & Stone, J.M. 1995, *ApJ*, 453, 332

Kraichnan, R.H., & Montgomery, D. 1979, *Rept. Prog. Phys.*, 43, 547

Matsui, Y., Long, K.S., Dickel, J.R., & Greisen, E.W. 1984, *ApJ*, 287, 295

Milne, D.K. 1987, *Aust. J. Phys.*, 40, 771

Reynolds, S.P. & Chevalier, R.A. 1981, *ApJ*, 245, 912

Stone, J.M. & Norman, M.L. 1992, *ApJS*, 80, 791

Strom, R.G. & Duin, R.M. 1973, *A&A*, 25, 351

Fig. 1.— A schematic representation of our computational domain (bold lines) for the simulation of young SNR. The sector $67.5^\circ \leq \theta, \phi \leq 112.5^\circ, 0 \leq r \leq 1.05r_{shock}$ is resolved with $200 \times 200 \times 180$ cells, with $200 \times 200 \times 100$ uniform cells tracking the shell (intershock region).

Fig. 2.— Grey scale images of the density field of the intershock region. Each image shows the density distribution at $t=100, 200, 300, 400,$ and 500 years from top to bottom. Left images are the results from a 2D simulation and the right images are slices of 3D simulation.

Fig. 3.— Angle-averaged magnitude of magnetic field at $t = 500$ years.

Fig. 4.— Evolution of each component of turbulent and magnetic energy density ($E_{tur} = \frac{\int \frac{1}{2} \rho |\vec{v} - \langle \vec{v} \rangle_{\theta, \phi}|^2 dV}{\int dV}$ and $E_{mag} = \frac{\int \frac{1}{8\pi} |\vec{B} - \langle \vec{B} \rangle_{\theta, \phi}|^2 dV}{\int dV}$).

Fig. 5.— Grey scale images of total radio intensity at four epochs : (a) $t=200$ yrs; (b) $t=300$ yrs; (c) $t=400$ yrs; (d) $t=500$ yrs.

Fig. 6.— Grey scale images of total radio intensity. (a) normal case, (b) switch-B case, (c) peculiar-B case.

Fig. 7.— The polarized intensity and the polarized magnetic field vectors for the normal case at $t=500$ years.

Fig. 8.— The polarized intensity and the polarized magnetic field vectors for the switch-B case at $t=500$ years.

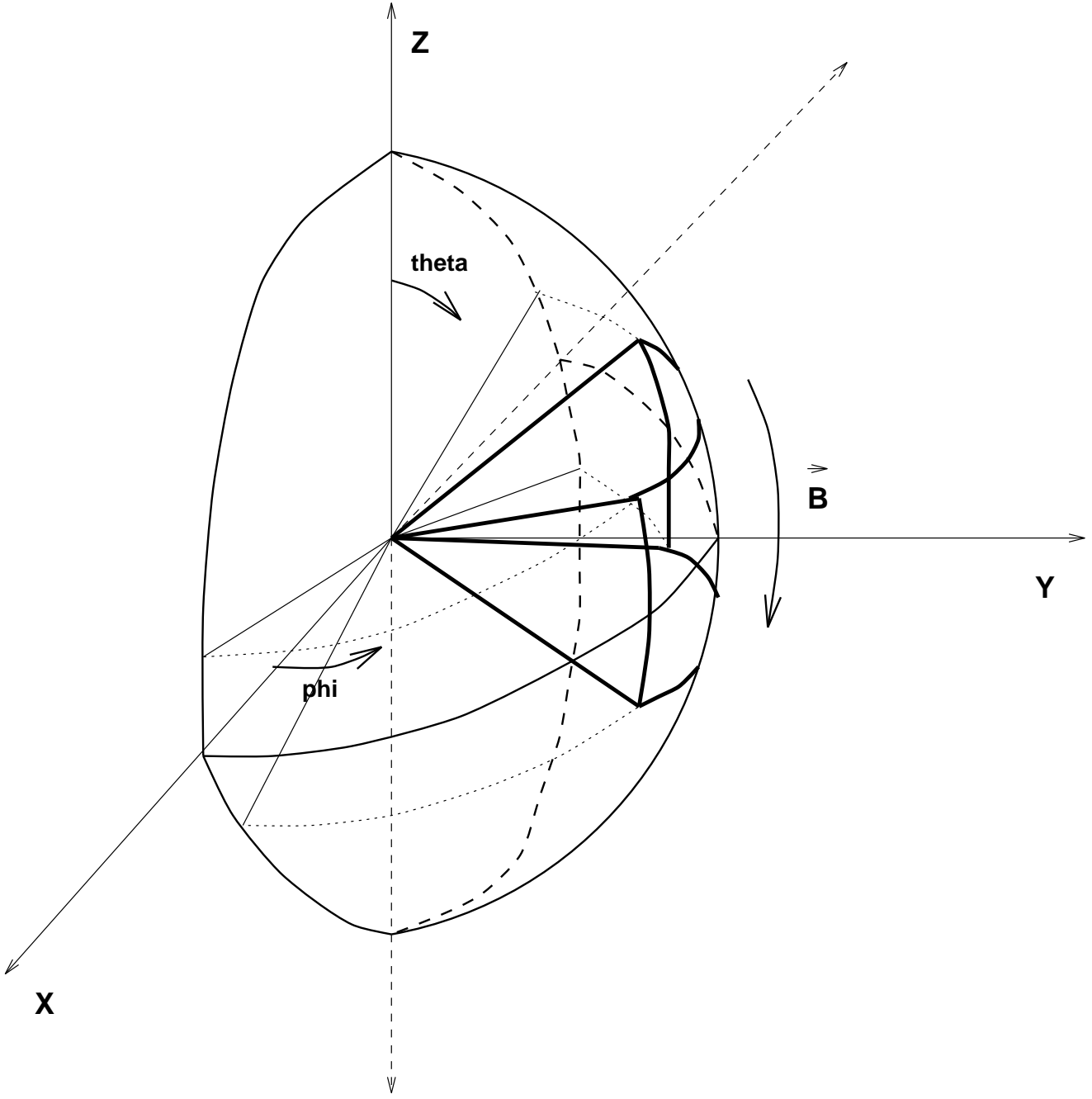
Fig. 9.— The polarized intensity and the polarized magnetic field vectors for peculiar-B case at $t=500$ years.

Fig. 10.— Polarized intensity vs. total intensity for peculiar-B case. I_{max} denotes the maximum total intensity.

Fig. 11.— Slices of the brightness distribution of the total intensity (left), the polarized intensity (middle), and fractional polarization (right) at $t=500$ years. Units for the total intensity and the polarized intensity are arbitrary.

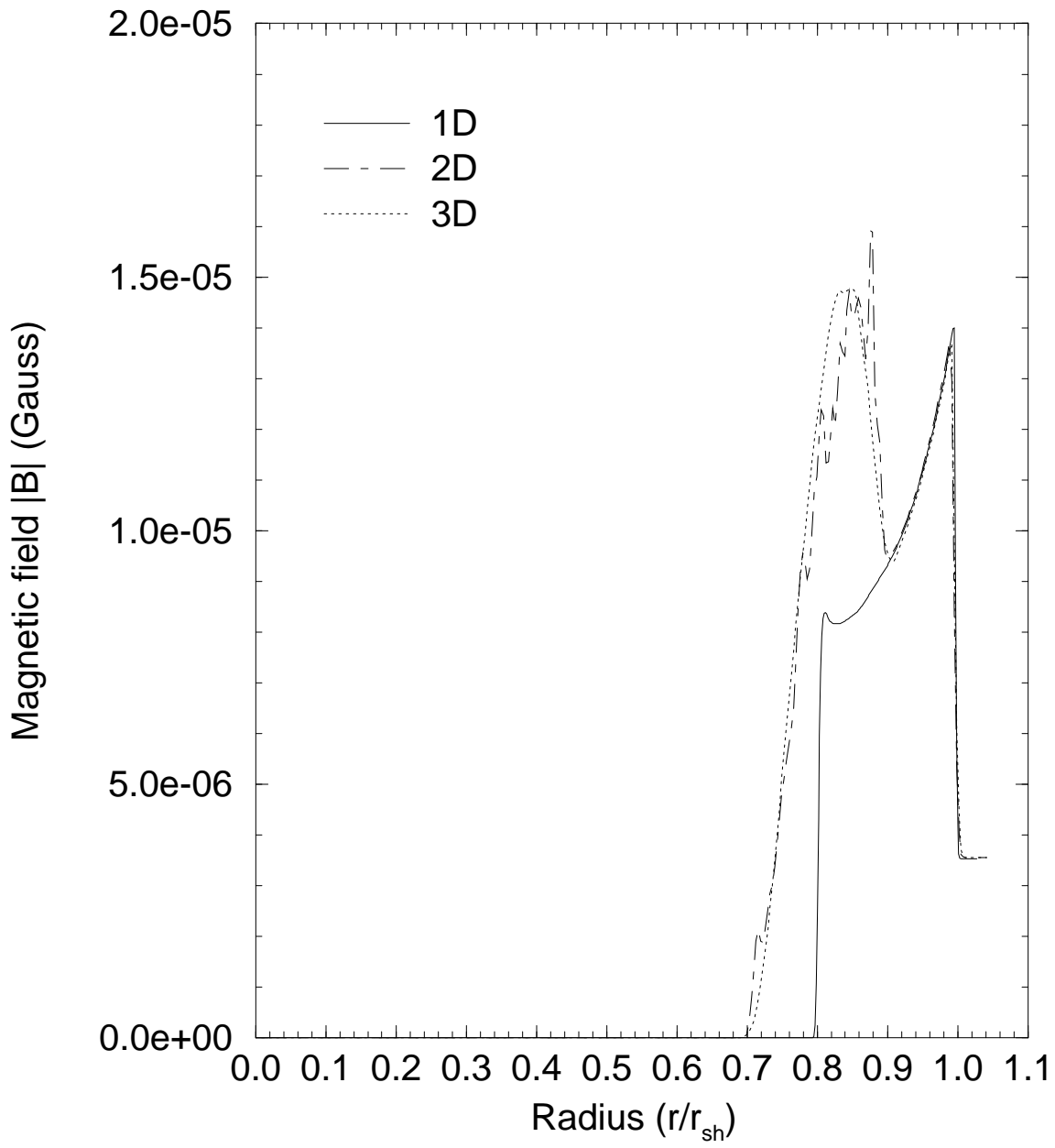
Fig. 12.— The time history of the radio luminosity computed from our computational space. $L_x, L_y,$ and L_z are the radio luminosity integrated along the X-direction, Y-direction, and Z-direction, respectively. $L_{x,\delta B}, L_{y,\delta B},$ and $L_{z,\delta B}$ are the radio luminosity integrated along X-direction, Y-direction, and Z-direction with the peculiar components of magnetic fields.

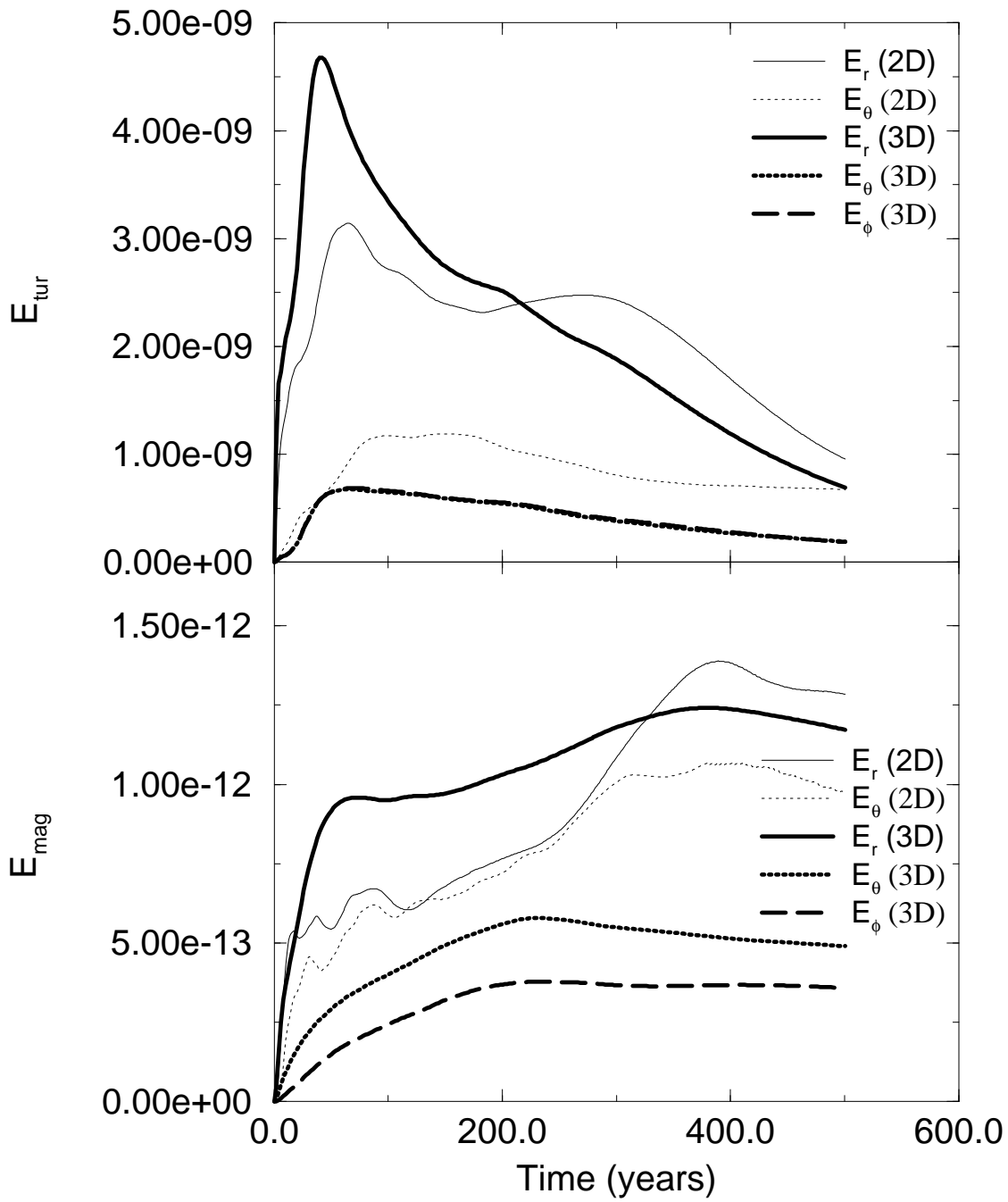
Fig. 13.— Grey scale images of the total intensity (top) and the polarized intensity overlaid with polarization B-vector (bottom) at $t=500$ years. Emissivity is computed by putting multiplication factor 5 to magnetic field components stronger than the shocked field.



This figure "snr3d_f02.jpg" is available in "jpg" format from:

<http://arxiv.org/ps/astro-ph/9606096v1>





This figure "snr3d_f05.jpg" is available in "jpg" format from:

<http://arxiv.org/ps/astro-ph/9606096v1>

This figure "snr3d_f06.jpg" is available in "jpg" format from:

<http://arxiv.org/ps/astro-ph/9606096v1>

This figure "snr3d_f07.jpg" is available in "jpg" format from:

<http://arxiv.org/ps/astro-ph/9606096v1>

This figure "snr3d_f08.jpg" is available in "jpg" format from:

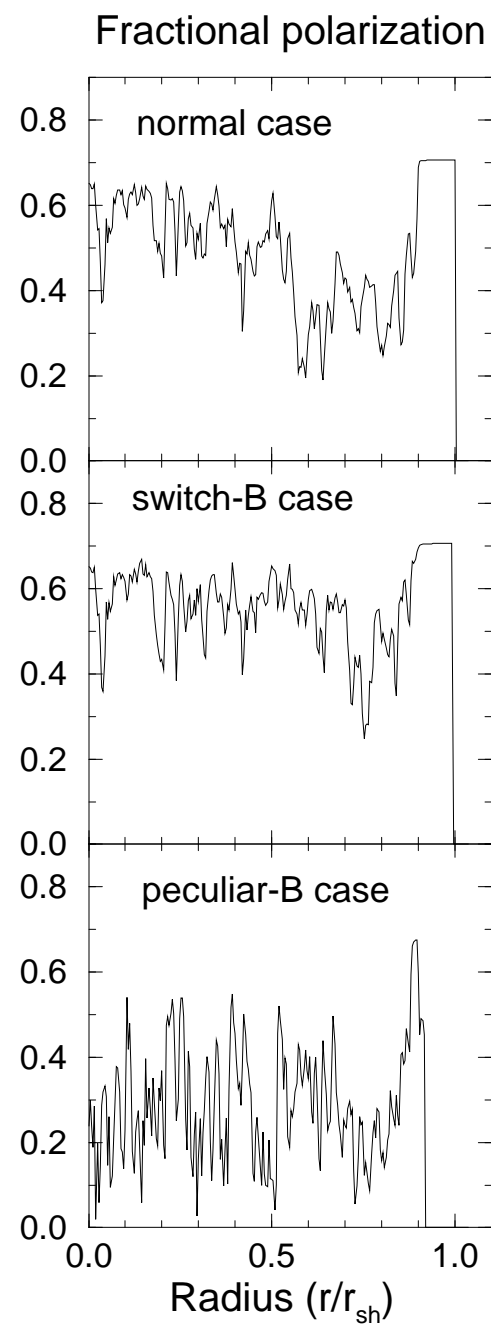
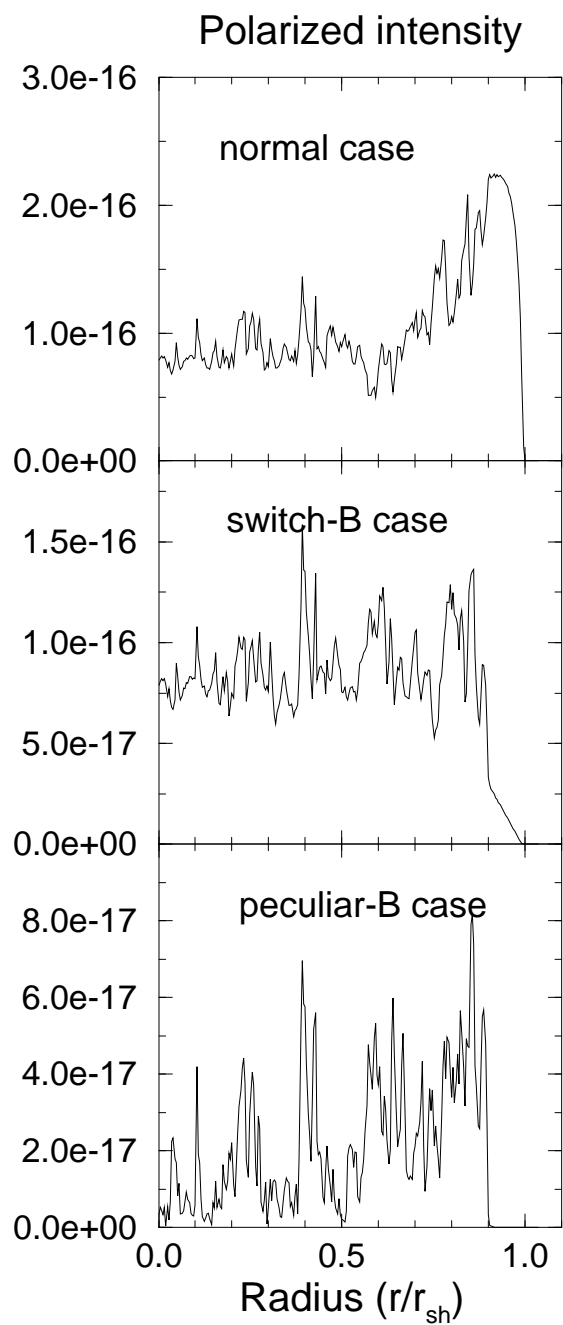
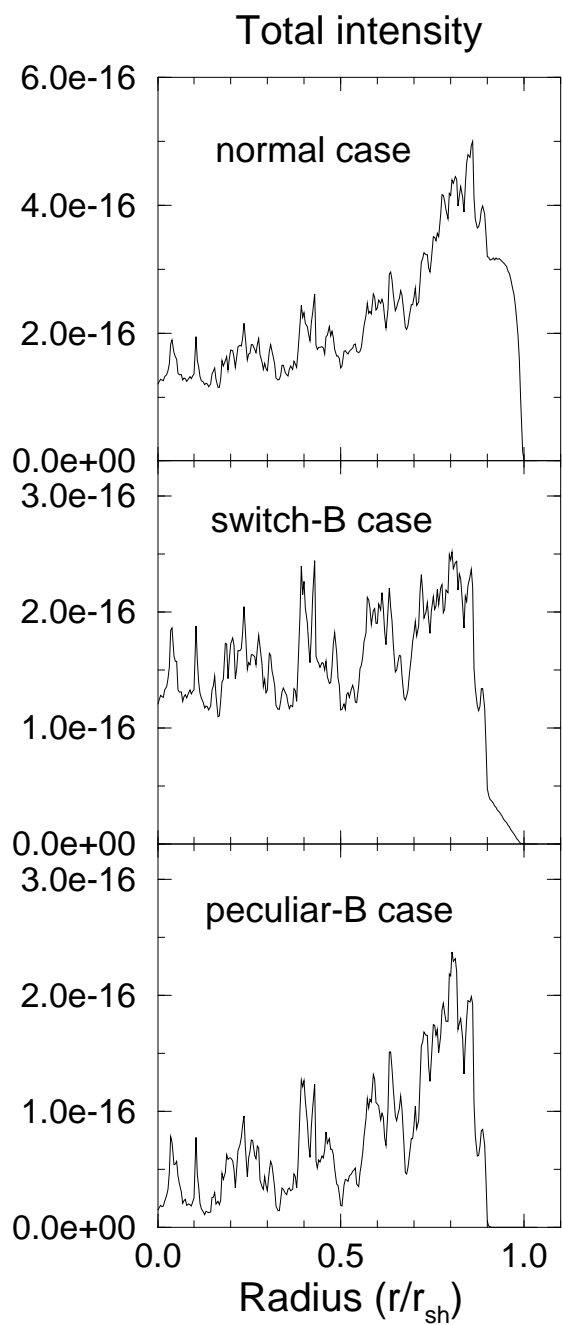
<http://arxiv.org/ps/astro-ph/9606096v1>

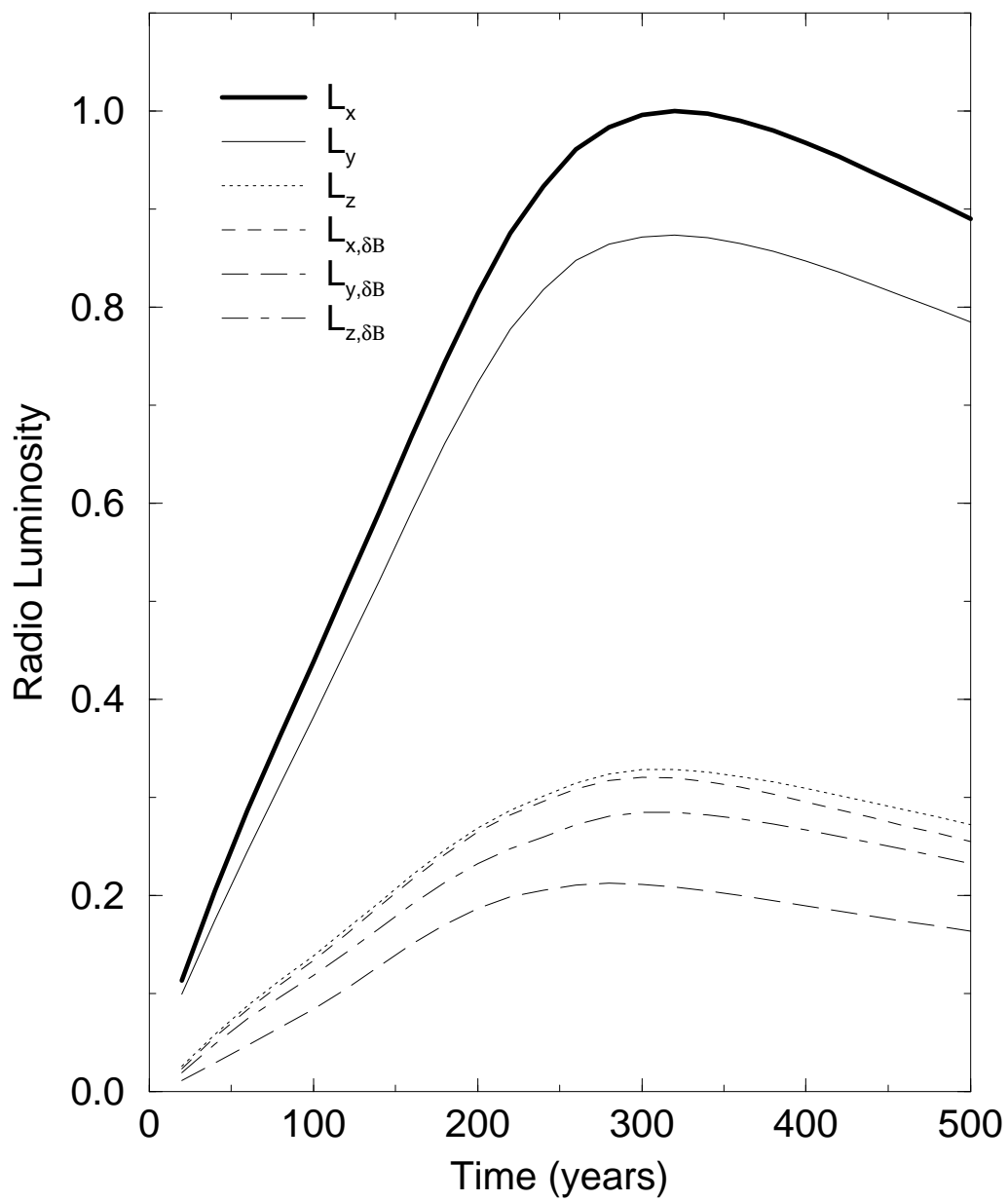
This figure "snr3d_f09.jpg" is available in "jpg" format from:

<http://arxiv.org/ps/astro-ph/9606096v1>

This figure "snr3d_f10.jpg" is available in "jpg" format from:

<http://arxiv.org/ps/astro-ph/9606096v1>





This figure "snr3d_f13.jpg" is available in "jpg" format from:

<http://arxiv.org/ps/astro-ph/9606096v1>